

Adsorption of Nitrogen on Mn(II) Metal-organic Framework Nanoparticles

Idongesit Justina Mbonu* and Olusegun Kehinde Abiola

Department of Chemistry, Federal University of Petroleum Resources, Effurun, Nigeria

Page | 4164

Date Received: 28-12-2020

Date Accepted: 01-04-2021

DOI: <https://doi.org/10.48198/NJPAS/20.B24>

ABSTRACT

Adsorption of N₂ on mixed ligand benzoic acid and 1, 10-phenanthroline ligands of Mn(II) metal-organic framework (MOF)-nanoparticles were demonstrated. The adsorption capacity and pore size distribution of the synthesized MOF were conducted experimentally by measuring the N₂ adsorption isotherm at 77.3 K. The resulting data were fitted to Brunauer-Emmett-Teller (BET), de Boer, Dubinin-Reduskevich (DR), Banet-Joyner-Halenda (BJH), Horvath-Kawazoe (HK) and Density Functional Theory (DFT) models to describe the adsorptive behaviour of the synthesized nanoparticles. The DSC analysis shows the high chemical stability of this compound. The FT-IR measurement reports present the abundant of highly coordinated functional groups. And the adsorption properties evaluated by different adsorption models compared with existing adsorbent materials suggest Mn-MOF with good thermal stability, high surface area and pore openings, is a promising material for storing gases and energy because at low or high pressures, it can adsorb nitrogen gas due to its large openings.

Keywords: Metal-organic framework, Mn-MOF Nanoparticles, Mn complex, Adsorption Studies

Introduction

Self-assembly (Chakrabarty *et al.*, 2011) methodology of synthesis can be a robust (Chakrabarty *et al.*, 2011) tool (Agthe *et al.*, 2015) for the preparation (Gawas *et al.*, 2012) of complex supramolecular (Sun *et al.*, 2018; Shoji *et al.*, 2019) architectures with fascinating properties. Self-assembly permits greater control (Chakrabarty *et al.*, 2011) in creating two and three-dimensional structures on account of predicting the way metal-ligand coordination

sphere (Jin *et al.*, 2014) and ligand liability direct the reactions (Ion *et al.*, 2015) to the desired products (Springer *et al.*, 2020). Nature utilizes different kinds of weak (Bandosz and Petit, 2011), noncovalent (Zhang, 2003) interactions (Jin *et al.*, 2014) like hydrogen (Guo *et al.*, 2016) bonding, charge-charge (Piota *et al.*, 2018), donor-acceptor (Bose *et al.*, 2019), π - π (Kupgan *et al.*, 2019), van der Waals (Jiang *et al.*, 2011), and hydrophilic and hydrophobic interactions (Zhao *et al.*, 2016), to

Corresponding Author: Idongesit Justina Mbonu

Department of Chemistry, Federal University of Petroleum Resources, Effurun, Nigeria.

. Phone: +2348037047734; Email: mbonu.idongesit@fupre.edu.ng



create self-assembled complex structures with controlled shapes (Wu *et al.*, 2017), and sizes (ChandanDey *et al.*, 2014). Self-assembly (Sun *et al.*, 2018) offers a wealth of understanding processes (Shoji *et al.*, 2019) like natural life fibers (Muhammad *et al.*, 2011; Seredych and Bandosz, 2012), micelles (Landers *et al.*, 2013), vesicles (Ravikovitch *et al.*, 2000), ribbons (Foo and Hameed, 2010), and tubes (Li-Hua and Peng-Fei, 2018).

Researches into complex useful organic molecules through dynamic (Agthe *et al.*, 2015) covalent bonding have brought out exploitable chemical and physical properties (Kumar *et al.*, 2016) of these molecules for exciting applications (Yu-Ling *et al.*, 2016) within the fields of energy (Shoji *et al.*, 2019) storage, gas (Li-Hua and Peng-Fei, 2018) adsorption, gas separation (Kumar *et al.*, 2016), host-guest chemistry (Jiang and Yaghi, 2015) and nanocomposite preparations (Lowell *et al.*, 2006). The metal ions in coordination polymers (Landers *et al.*, 2012) are the sources of the energy storage, magnetism, luminescence (Kupgan *et al.*, 2019), and adsorption within the compound (Lv *et al.*, 2015). Tailoring functionality to meet required luminescence (Gawas *et al.*, 2012), electronic, mechanical (Sasmal *et al.*, 2019) and optical properties need careful control over numerous components for the formation of self-assembled coordination (Landers *et al.*, 2012) polymers.

This account focuses on the investigation of the adsorption (Mokhat and Mak, 2019) capacity of the manganese (II) supramolecular reaction induced by the benzoate ion and 1,10-phenanthroline ligands rearrangement. The two hemilabile ligands possessing different binding sites reacted with manganese metal ions resulting in a heteroligated complex compound with enhanced adsorption capacity for various applications in luminescence and energy storage (Shoji *et al.*, 2019).

In this present work, we established how porous Mn-MOF adsorb nitrogen and can be used for

storing energy through comparing theoretical breakthrough curves with the experimental observed results (Piota *et al.*, 2018; Wu *et al.*, 2017). The prepared Mn-MOF builds out as crystal in all directions exhibiting a very rigid, uniform, and precise arrangement of atoms with six-coordinate manganese (II) centers as the primary metal node. The carboxylate ligands adopt monodentate and bidentate coordination mode. Because of their affinity for oxygen atoms, they are often used to synthesize functional metal complexes. 1, 10-phenanthroline was incorporated to the backbone of the carboxylate ligand to prevent the coordination of more water molecules with the manganese(II) metal ions.

The electronic properties of this six-coordinate Mn(II) center make this MOF reactive towards nitrogen, creating a stronger M-N₂ interaction. The coordination sites saturated with Mn-MOF nanoparticles cannot interact with nitrogen gases (Foo and Hameed, 2010) easily. The high-density of Mn(II) shows a high gas uptake capacity, making Mn-MOF a promising N₂ adsorbent (Yu-Ling *et al.*, 2016) capacity for various applications in the areas of luminescence and energy storage (Shoji *et al.*, 2019). Different Adsorption isotherm models (Foo and Hameed, 2010) were used to evaluate the adsorption (Yu-Ling *et al.*, 2016) capacity of the Mn-MOF and its pore filling towards applications for adsorbent-based chillers, heat pumps, and gas storage (Bandosz and Petit, 2011; Christian *et al.*, 2016).

Materials and Methods

All the chemicals utilized in this work are of reagent grade (Petit and Bandosz, 2011) and used as obtained. The elemental composition of Mn-MOF was performed on Perkin-Elmer 2400 elemental analyzer. Morphology of the prepared compound was carried out on a Zeiss Supra (Christian *et al.*, 2016) instrument with a resolution of 5 nm at 30 kV (Petit and Bandosz, 2011). Vibration bands within Mn-MOF were determined using a Nicolet Magna

(Oluwaniyi *et al.*, 2016) FT-IR spectrometer within the range of 400–4000 cm^{-1} .

The surface area, pore size, and pore diameter of the Mn-MOF were evaluated by measuring the N_2 adsorption isotherms (Kupgan *et al.*, 2019) at "77.3 K" using an iQMicropore-XR (Quantachrome Instruments, FL, USA). Prior to the experiment, the sample was outgassed (Yu-Ling *et al.*, 2016) under vacuum at 120 °C (PalSharma *et al.*, 2009).

A single crystal Mn-MOF (0.05 mm x 0.54 mm x 0.60 mm) was selected and mounted on a cryoloop for structure determination on a Bruker DUO APEX II CCD diffractometer using graphite-monochromatic $\text{MoK}\alpha$ ($\lambda = 0.71073 \text{ \AA}$) Oxford Cryostream-700. The structure was solved by a direct method in SHELXT-2018/3 (Tahier and Oliver, 2015).

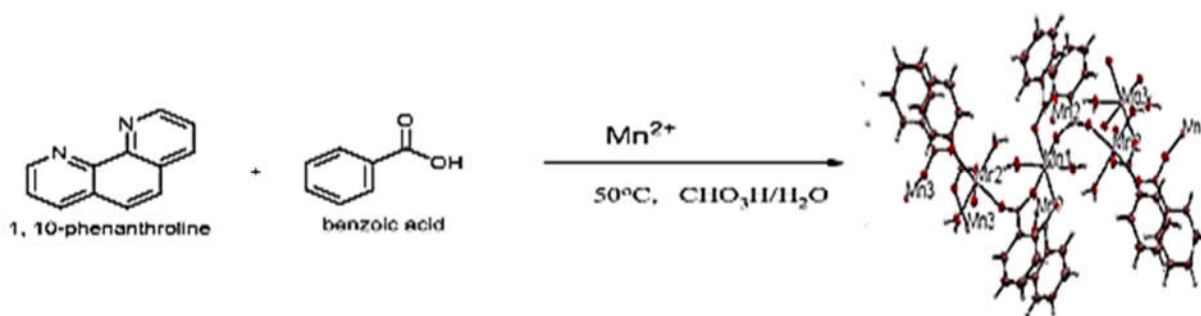


Figure 1: Graphical reaction pathway to Mn-MOF nanoparticles

Results

The one-pot synthesis of yellow Mn-MOF single crystal analysis in Fig. 2a shows a 3D microporous supramolecular network constructed by 2D-layered Mn-MOF with related crystallographic data (Bandosz and Petit, 2011) listed in Table 1. Diffractogram in Fig. 2b & c shows that the Mn-MOF crystallized in a triclinic space group P-1 (Yu-Ling *et al.*, 2016). The asymmetric unit displayed a monodentate benzoate ligand, two 1, 10-Phenanthroline ligands, a coordinated water molecule. The Mn(II) ion is six coordinated

Self-assembly of Mn-MOF nanoparticles

Mn-MOF was prepared as shown in Figure 1. The mixture of $\text{MnCl}_2 \cdot 4\text{H}_2\text{O}$ (0.5 mmol) and benzoic acid (0.1 mmol) in 20 mL aqueous solution was stirred for 5 minutes at 50 °C. NaOH (1mol/L) solution was used to maintain the hydrogen ion concentration of the reaction mixture. A 5 mL alcohol solution of 1, 10-phenanthroline (1.5 mmol) was added with stirring for 3 hours at 50 °C. On the fifth day, pale yellow crystals were observed to have separated from the mother liquor in a reaction vessel (Mbonu *et al.*, 2020; Tahier and Oliver, 2015). The elemental analysis result shows that the C, H, Mn, and O are 50.50, 4.20, 16.50, and 28.80 (calc.) and 50.48, 4.27, 16.40, and 28.85 (found), respectively.

(Christian *et al.*, 2016) by four nitrogen atoms from two (Christian *et al.*, 2016) 1,10-Phenanthroline ligands, one oxygen atom (Zhao *et al.*, 2016) from the carboxylate group of benzoate ligand, and one oxygen atom (Yu-Ling *et al.*, 2016) from coordinated water molecule resulting in a distorted octahedral shape. Neighboring benzoate and phen groups are interlinked through π - π stacking interactions (Jiang and Yaghi, 2015).

SEM micrograph presented in Figure 3 depicts the texture of the Mn(II)-MOF studied, to be plate-like sizes formed into larger particles. The morphology

analysis (Guo *et al.*, 2016) revealed that the Mn-MOF is porous with a total surface area having many mesoporous pores, and a good nitrogen adsorption performance is expected of the porous Mn-MOF (Lowell *et al.*, 2006). The fluorescence spectrum in Figure 4, measured within the range of 300-800 nm is shifted to a longer wavelength with an emission maximum of 400 nm (Li-Hua and Peng-Fei, 2018).

An infrared spectrum of Mn-MOF in figure 5, shows vibration bands within the range (Kupgan *et al.*, 2019) of 3100-3753 cm^{-1} for $\nu(\text{OH})$ (Kupgan *et al.*, 2019) and 842–920 cm^{-1} for $\sigma(\text{OH})$ (Kupgan *et al.*, 2019) an indication of coordinated water (Kupgan *et al.*, 2019) in Mn-MOF. The complex exhibits N-H stretching within the range of 2753-3373 cm^{-1} . The asymmetric and symmetric stretching frequencies of carboxylate (Sasmal *et al.*, 2019) ions are shown within the range of 1688-1618 cm^{-1} and 1416-1282 cm^{-1} (Foo and Hameed, 2010). The characteristic IR bands of Mn(II) complex appears at 1688 cm^{-1} (C=O) [30] and 3373 cm^{-1} (H_2O) (Li-Hua and Peng-Fei 2018). The N-N stretching frequency (Sasmal *et al.*, 2019) of the complex appeared at 779-708 cm^{-1} (Sasmal *et al.*, 2019) is associated with bidentate bridging nature of neutral ligands. These results are an indication that Mn-MOF was successfully synthesized.

Figure 6 shows the Brunauer-Emmett-Teller (BET) single- multilayer adsorption/desorption isotherms plot of Mn-MOF at 77.3 K (Table 2). The correlation coefficient ($R^2 = 0.992$) and surface area using the BET model was determined by the following linear expression in Eq. 1 (Foo and Hameed, 2010):

$$\frac{1}{W\left[\left(\frac{P_0}{P}\right)-1\right]} = \frac{1}{W_m C} + \frac{C-1}{W_m C} \left(\frac{P_0}{P}\right) \quad (1)$$

Where W = weight of gas adsorbed, P/P_0 = relative pressure, W_m = weight of adsorbate as a monolayer, C = BET constant. Slope (s), intercept (i), and weight (W_m) were determined from Eq.2 below:

$$s = \frac{C-1}{W_m C} i = \frac{1}{W_m C} W_m = \frac{1}{s+i} \quad (2)$$

Total surface area (S_t) was calculated from expression (Eq.3):

$$S_t = \frac{W_m N A_{cs}}{M} \quad (3)$$

N = Avogadro's number (6.023×10^{23}), M = Molecular weight of Adsorbate (28.013), A_{cs} = Adsorbate cross-sectional area (16.2 \AA^2 for Nitrogen). Specific Surface Area (S) (Li-Hua and Peng-Fei, 2018) is then determined by the total surface area Li-Hua and Peng-Fei, 2018) by sample weight in Eq. 4:

$$S = \frac{S_t}{W} \quad (4)$$

The experimentally determined surface area with the BET model = $825.465 \text{ m}^2 \text{ g}^{-1}$ which is large compared to some natural porous (Muhammad *et al.*, 2011) materials, such as clay ($10\text{-}100 \text{ m}^2 \text{ g}^{-1}$) (Seredych and Bandosz, 2012), activated graphite ($119 \text{ m}^2 \text{ g}^{-1}$) and other types of zeolite and porous carbons (Muhammad *et al.*, 2011; Li-Hua and Peng-Fei, 2018).

Langmuir's experimental data plot (Fig. 7) features a broader plateau region of the loop, which extends up to relatively high P/P_0 . The optimization of relative pressure within the range of $0.00\text{E}+00$ - $3.50\text{E}-02$ in Fig. 7 shows, adsorption increased with increasing relative pressure and at 1.71 the adsorption process was maximum with 84.62 % and then slightly decreases and practically constant till relative pressure $3.00\text{E}-01$. The lesser adsorption at lower relative pressure could be attributed to lesser surface sites available for sorption (Foo and Hameed, 2010). This model was used to investigate the sorption capacity of Mn-MOF using the linear expression in equation 3:

$$\frac{1}{V_a \left[\frac{P_0}{P} - 1 \right]} = \frac{C-1}{V_m C} X \frac{P}{P_0} + \frac{1}{V_m C} \quad (5)$$

Where P = partial vapour pressure (Oluwaniyi *et al.*, 2013) of adsorbate, P_0 = saturated pressure of adsorbate.

Figure 8 isotherm plot of volume at STP (cc/g) against relative pressure shows a linear fitting result with a strong correlation of +1 indicating a perfect positive linear relationship. The estimated micropore volume of Mn-MOF from this model is found to be 5.151cc/g (Jiang *et al.*, 2011).

Figure 9 shows a linear correlation between the volumes adsorbed with statistical thickness. The t values were determined using Halsey equation in Eq.6 &7 (Lowell *et al.*, 2006):

$$t(\text{\AA}) = \left[\frac{13.99}{0.034 - \log \frac{P}{P_0}} \right]^{0.5} \quad (6)$$

$$t = \frac{V_{liq}}{S} \times 10^4 (\text{\AA}) \quad (7)$$

Where S is the total surface area (Lowell *et al.*, 2006) and V_{liq} is the adsorbed liquid volume (Lv *et al.*, 2015); $V_{liq} = V_{ads} (STP) \times 15.47$ for nitrogen adsorption at 77.3 K (Lowell *et al.*, 2006). The T-method for external surface area analysis calculated from the slope (Eq.1) give surface area comparable to BET values (Sasmal *et al.*, 2019) showing an agreement between the two methods.

Dubinin-Radushkevch (DR)-plot by expression (4) gave information on the micropore volume (Kupgan *et al.*, 2018). The shape of the experimental Logarithm weight adsorbed plot against $\log^2 P/P_0$ (Fig. 10) results in a linear uniform Gaussian distribution with a negative intercept and negative slope. The adsorption energy, average pore width, micropore volume, and micropore surface area of the Mn-MOF were determined from Eq. 8, Table 2 (Kumar *et al.*, 2016).

$$W = W_0 \exp \left[- \left(\frac{A}{\beta E_0} \right)^2 \right] \quad (8)$$

$$A = - \Delta G = RT \ln \left(\frac{P_0}{P} \right), E = \beta E_0$$

Where, β =affinity coefficient (0.3300), A = adsorption potential, DR $\exp(n) = 2.000$, E = Characteristic adsorption energy, W and W_0 are

amount adsorbed at P/P₀ and the micropore volume, respectively.

The PSD (Table 3) from the experimental adsorption (Landers *et al.*, 2013) isotherm $N_{exp} \left(\frac{P}{P_0} \right)$ were determined from equation 9 (Landers *et al.*, 2013). The experimental isotherm (Table 3) is represented in Figures 11a & b as differential (left) and cumulative (right) distributions. Figure 11b shows pore size distribution (Ravikovitch *et al.*, 2000) calculated by QSDFT and NLDFT (Foo and Hameed, 2010) methods to overlap generously indicating that despite different approaches both methods give similar results. Both methods show the three-peak distribution of micropores region with sizes 1.93 and 2.31-2.64 nm. The lowest pore size on QSDFT PSD as expressed in Eq. 9 is 1.68 nm resulting in not fully resolved peak in low pore size range with an L-curve (Lv *et al.*, 2015)

$$N_{exp} \left(\frac{P}{P_0} \right) = \int_{D_{min}}^{D_{max}} N_{QSDFT} \left(\frac{P}{P_0}, D \right) F(D) dD \quad (9)$$

Where: $N \left(\frac{P}{P_0} \right)$ = experimental adsorption isotherm data, W = pore width, $N \left(\frac{P}{P_0}, W \right)$ = isotherm on a single pore of width W, f(W) = pore size distribution function. Here D_{min} and D_{max} are the minimum and maximum pore sizes (Yu-Ling *et al.*, 2016) in the kernel, respectively.

Figure 11. (a) Cumulative (Landers *et al.*, 2013) and (b) Differential cumulative pore volume (Seredyc and Bandosz, 2012) and cumulative surface area distributions of Mn -MOF on carbon slit pore from N₂ adsorption isotherms at 77.3 K (Seredyc and Bandosz, 2012) using NLDFT equilibrium mode.

Figure 12: (a) shows the ore size distribution and (b) shows the DSC plot with a depression at 264.43 °C (− 7.20 mW), $\Delta H +107.00$ KJ/mol ($\Delta H +551.00$ J/g).

Table 4 gives the micropore analysis by Dubinin-Radushkevich (DR), Horvath-Kawazoe (HK), and

Dubinin-Astakhov (DA) Methods. Dollimore and Heal (DH) (Landers *et al.*, 2013) were used to estimate the pore size distribution (Kupgan *et al.*,

2018). The pore-size distribution (Muhammad *et al.*, 2011) is obtained by application of the BJH (Barret, Joyner, and Halenda) technique.

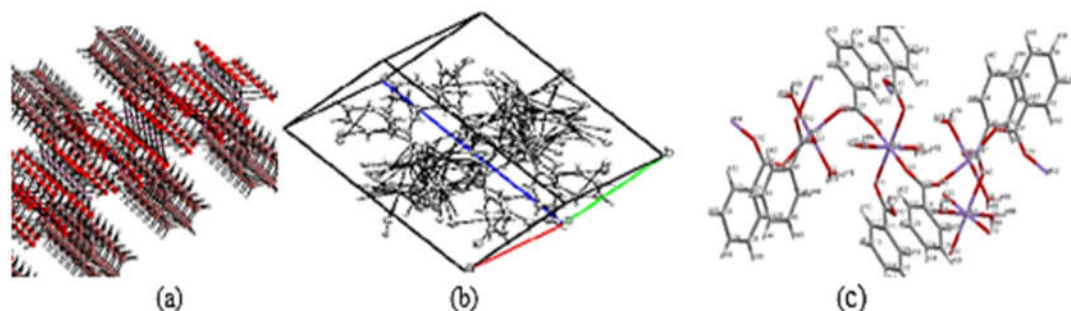


Figure 2: (a) Projection along 'a' axis of the three-dimensional framework showing the cavities (b) Molecular packing along the b axis (c) ORTEP drawing of Mn-MOF

Table 1: Crystal data, data collections and refinement of Mn(II)-MOF at 200 K

Crystal Data	
Empirical formula	C ₂₈ H ₂₈ Mn ₂ O ₁₂
Formula weight	666.38
Unit Cell Weight	1332.77 [Based on SHELXL2014 Atomic Weights]
Crystal system	Triclinic
Space group	P-1(No.2)
<i>a</i> /Å, α /°	7.4369(3), 88.847(2)
<i>b</i> /Å, β /°	12.9898(6), 82.518(2)
<i>c</i> /Å, γ /°	14.1176(6), 89.975(2)
Volume/Å ³	1351.93(10)
<i>Z</i>	2
ρ calc/g cm ⁻³	1.637
μ /mm ⁻¹	1.001
<i>F</i> (000)	684 [calc. 685.70]
Crystal size/mm ³	0.05 x 0.54 x 0.60
Wavelength/Å	
Data Collection	
Temperature/K	200
Theta Min-Max/°	1.6, 28.4
Dataset /restraints/parameters	-9: 9; -16: 17; -18: 18
Tot., Uniq. Data, R(int)	49223, 6713, 0.025
Observed Data [<i>I</i> ≥ 2.0σ(<i>I</i>)]	5021
Refinement	
Nref, Npar	6713, 414
R, wR2, S	0.0353, 0.1092, 1.05
w = $\frac{1}{\sigma^2(F_o^2) + (0.0551P)^2 + 1.0319P}$ Where	
P = $\frac{(F_o^2 + 2F_c^2)}{3}$	
Max. and Av. Shift/Error	0.00, 0.00
Min. and Max. Resd. Dens. [e/Å ³]	-0.56, 1.34
Radiation/ Å MoK α	0.71073

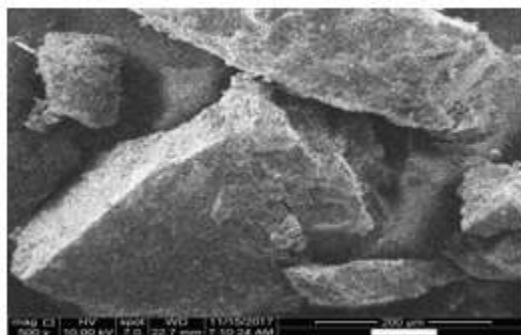


Figure 3: SEM micrograph of Mn-MOF

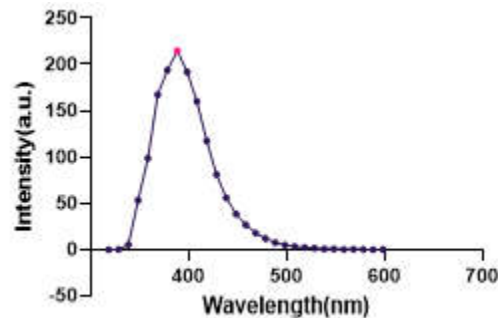


Figure 4: Fluorescence emission spectrum monitored at $\lambda_{ex} = 308 \text{ nm}$

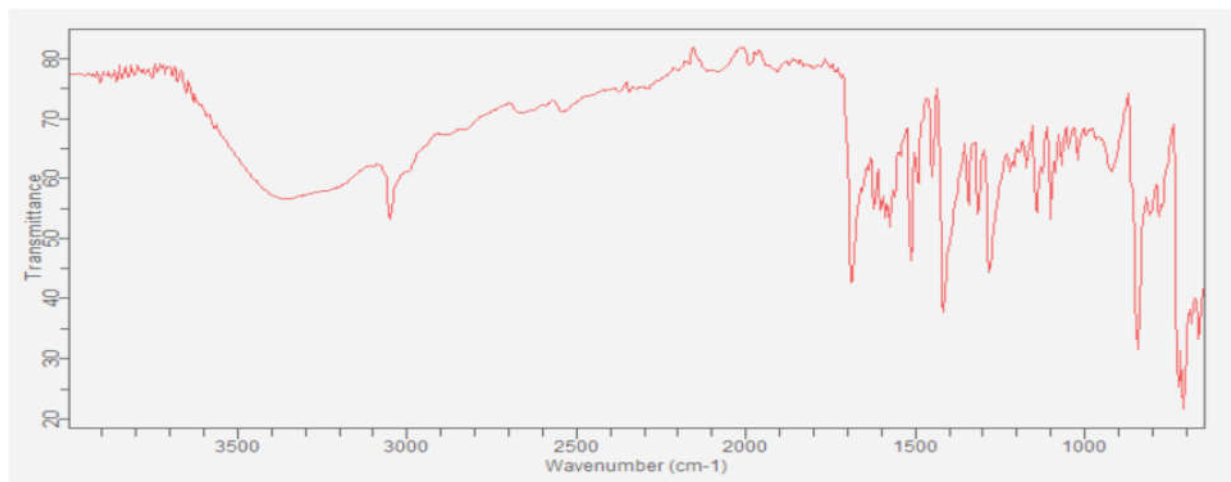


Figure 5: FT-IR spectrum of Mn-MOF

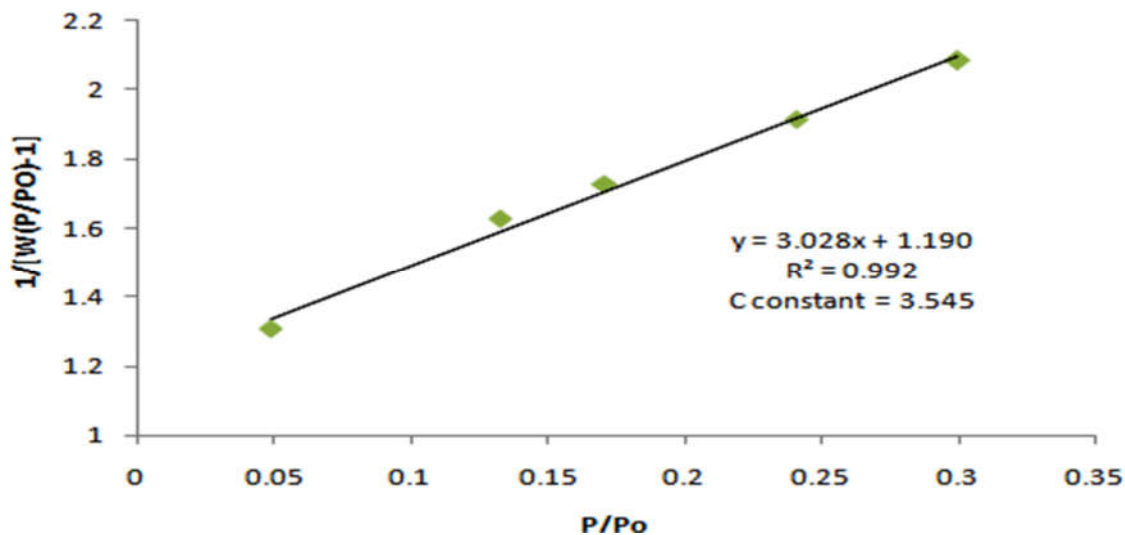


Figure 6: BET Single-multilayer nitrogen adsorption isotherm of Mn-MOF

Table 2: Nitrogen adsorption on Mn-MOF

P/Po	Volume at STP (cc/g)	1/[W(Po/P)-1]	P/Po/W	Log ₂ (P/Po)	Weight adsorbed [(g)]	Statistical thickness, Å
4.85E-02	31.2535	1.31E+00	1.24E+00	1.73E+00	4.69E-03	3.221736914
1.33E-01	75.3158	1.63E+00	1.41E+00	7.69E-01	1.13E-02	3.919188098
1.71E-01	95.5990	1.73E+00	1.43E+00	5.88E-01	1.43E-02	4.179641641
2.41E-01	132.8608	1.91E+00	1.45E+00	3.82E-01	1.99E-02	4.633363309
3.00E-01	164.7080	2.08E+00	1.46E+00	2.73E-01	2.47E-02	5.013433024

Table 3: DFT & NDFLT Pore Analysis

Pore width [nm]	Cumulative pore volume [cc/g]	Cumulative surface area [m ² /g]	dv(d) [cc/nm/g]	ds(d) [m ² /nm/g]
1.6879	0.00E+00	0.00E+00	0.00E+00	0.00E+00
1.7656	0.00E+00	0.00E+00	0.00E+00	0.00E+00
1.8469	5.23E-03	5.66E+00	6.43E-02	6.96E+01
1.9319	2.10E-02	2.20E+01	1.85E-01	1.92E+02
2.0208	3.50E-02	3.59E+01	1.58E-01	1.56E+02
2.1138	3.64E-02	3.72E+01	1.51E-02	1.43E+01
2.2111	5.49E-02	5.39E+01	1.90E-01	1.72E+02
2.3129	8.87E-02	8.31E+01	3.32E-01	2.87E+02
2.4194	1.19E-01	1.08E+02	2.84E-01	2.35E+02
2.5307	1.56E-01	1.38E+02	3.36E-01	2.65E+02
2.6472	2.02E-01	1.72E+02	3.90E-01	2.95E+02
2.7691	2.36E-01	1.97E+02	2.83E-01	2.05E+02

Table 4: Adsorption properties of Mn-MOF given by different Isotherm Models

Adsorption Models	Surface Area (m ² g ⁻¹)	Pore Size (nm)	Pore Volume ccg ⁻¹	Slope	Adsorption energy KJ/mol	C constant	Average pore width (nm)	Pore Diameter (nm)	Intercept	Best n	R ²
SinglePoint BET	5.017 E+02			3.029					1.190 E+00		0.9960
MultiPoint BET	8.255 E+02			3.029		3.545			1.190 E+00		
Langmuir	4.374 E+03			0.7961 2					1.25689		0.8650
Barrett, Joyner, and Halenda Method (BJH)	9.570 E+02	2.093	4.614 E-01						2.093 E+00		
Dollimore and Heal (DH)	1.034 E+03	2.093	4.776 E-01						2.093 E+00		
T-method	8.255 E+02										0.9940
Dubinin Radushkevich method (DR)	8.601E+02	6.077	3.056 E-01	-4.780 E-01	4.279		6.077 E+00		2.964E-02	2.000	0.9770
Density Functional Theory (DFT)	196.913		0.236						2.647		
Dubinin-Astakhov Method (DA)		2.920			0.707		2.920 E+00		2.964E-02	1.000	
Horvath-Kawazoe (HK)		1.882	1.326 E-01						1.882 E+00		
SF		3.534	2.708 E-02						3.534 E+00		

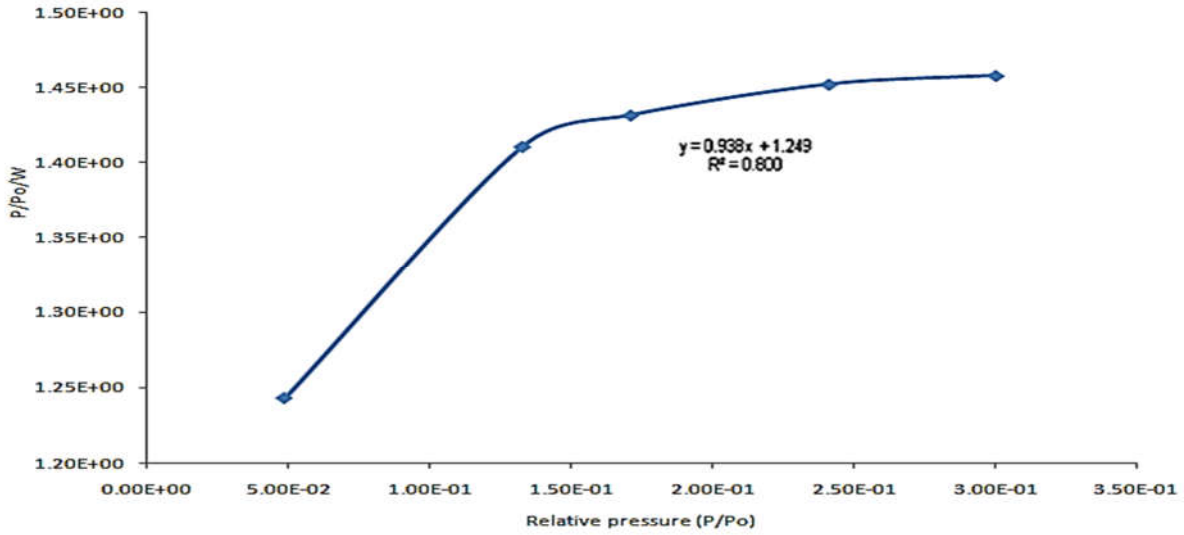


Figure 7: Langmuir plot of N₂ on Mn-MOF at 77.3K

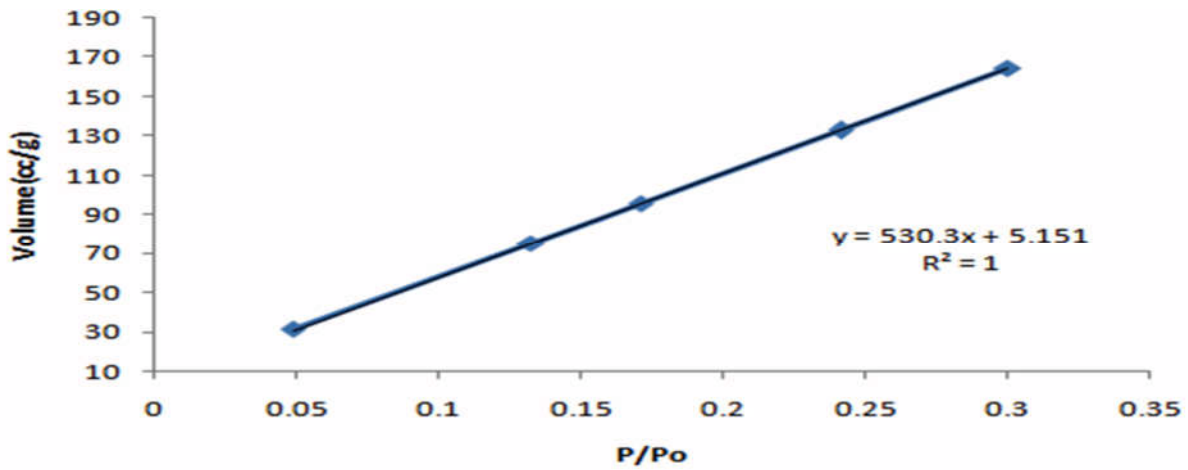


Figure 8: A linear form of Langmuir isotherm

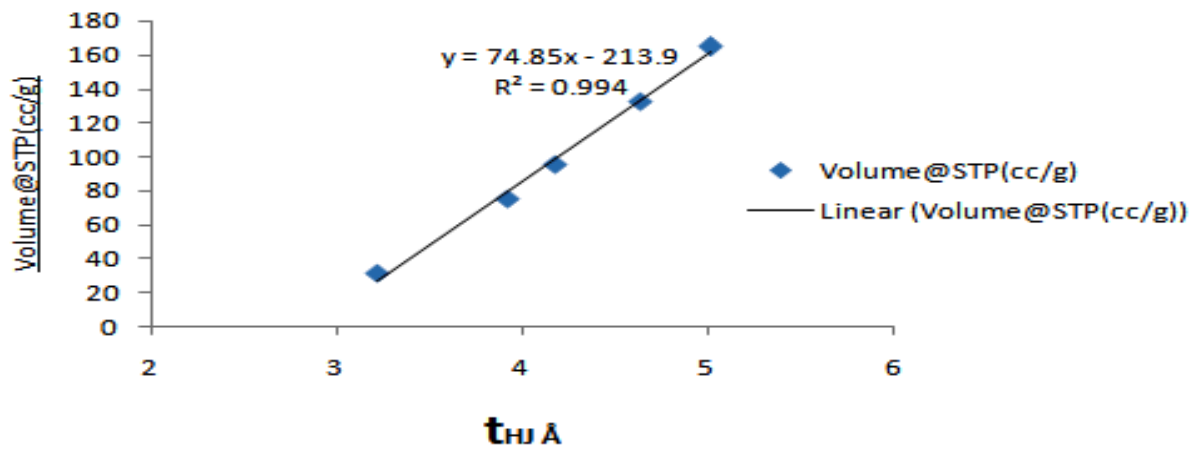


Figure 9: Temkin Adsorption isotherm for Mn-MOF

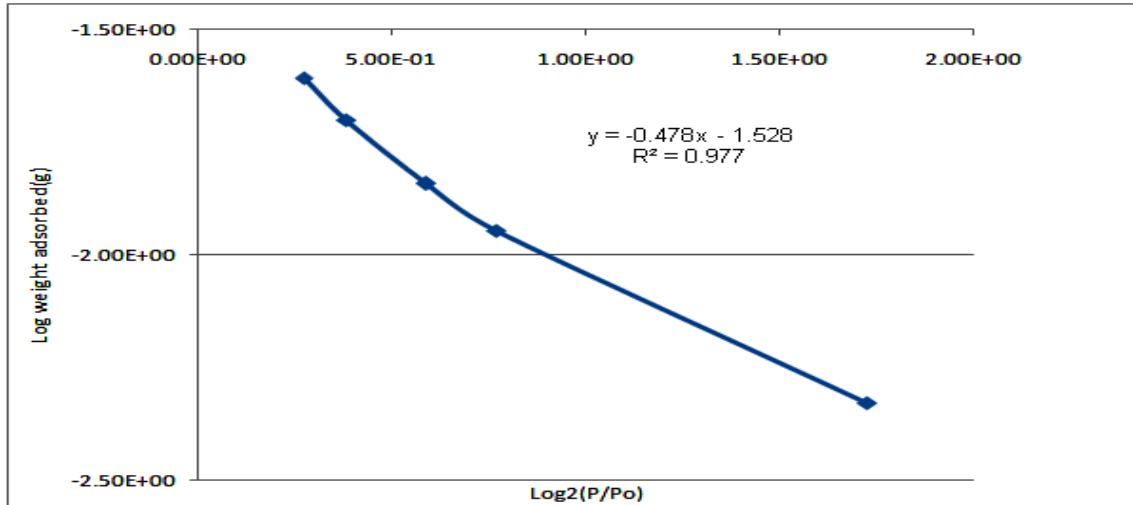


Figure 10: Dubinin-Radushkevich Adsorption isotherm for Mn-MOF

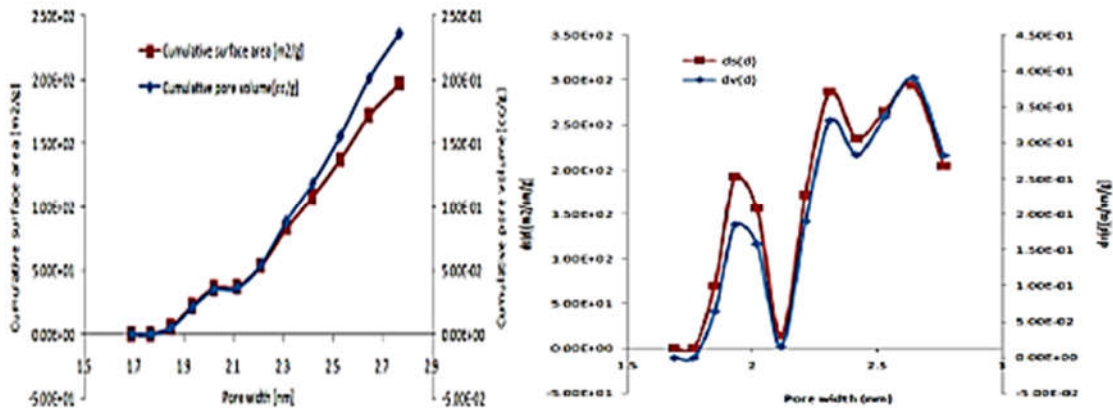


Figure 11: (a) Cumulative and (b) Differential cumulative pore volume and cumulative surface area distributions of Mn-MOF on carbon slit pore using NLDFT equilibrium mode

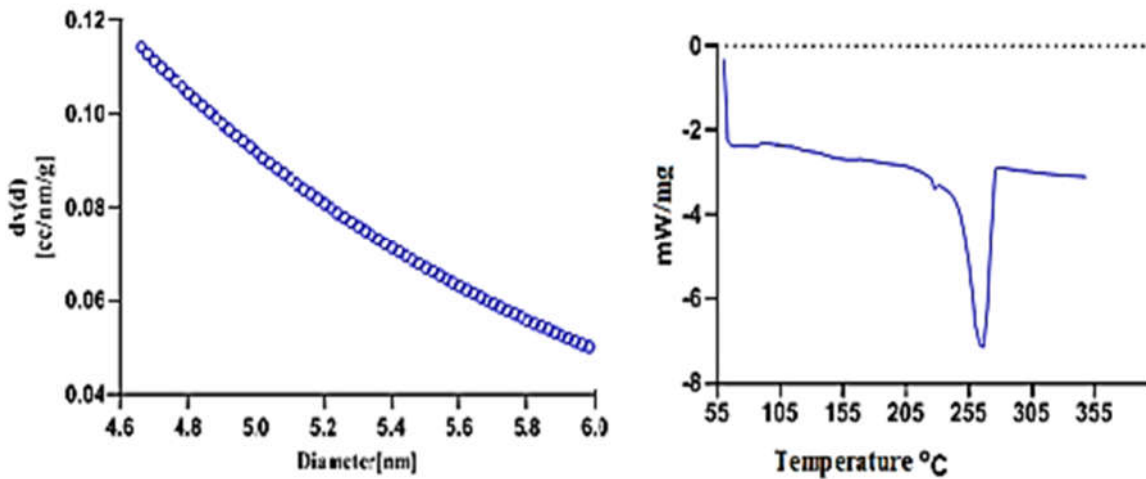


Figure 12 a and b: (a) NLDFT QSDFT Pore size distributions of Mn-MOF to nitrogen adsorption (b) DSC spectrogram of Mn-MOF

Discussion

The Langmuir surface area of 4374 m²g⁻¹ after activation, shows a high permanent porosity with an octahedrally coordinated environment. FT-IR spectrum results shows Mn-MOF has a well populated functional groups that form strong network of coordination for storage purposes. The Mn-MOF exhibits pore size 6.077 nm and pore volume of 2.920 nm displaying highly porous and high uptake capacity of a nitrogen.

Conclusions and recommendations

These results, agree with literature reviews performed, with adsorption studies published by numerous authors demonstrating the adsorption capacity of metal-organic frameworks for storage applications. This work presents an alternative synthetic method for preparing self-assembly porous metal-organic complexes with potential properties for nitrogen storage.

In this work, we employ several adsorption isotherms in investigating the adsorption capacity of the Mn-MOF synthesized. We used DSC, SEM, Single-crystal diffraction studies, FTIR, Fluorescence and UV-visible spectroscopy to characterize this compound. The experimental results obtained and evaluation of the different adsorption behaviours of the manganese(II) nanoparticles under some adsorption isotherms reveal the high adsorption capacity of this compound. We are currently trying to optimize the surface area of the Mn-MOF for hydrogen and carbon capture.

Competing interests

Authors have declared that no competing interests exist.

Authors' contribution

This work was carried out in collaboration between both authors. IJM designed the study, carried out analyses. IJM and KOA wrote the manuscript for publication

Funding

This work was supported by the Tertiary Education Trust Fund (RE: FUPRE/TO/RESR /2017/01), Nigeria.

Acknowledgments

The authors wish to acknowledge single-crystal structure analysis by Summerstrand Campus South, northwest University South Africa.

References

- Agthe, M., Hoydalsvik, K., Mayence, A., Karvinen, P., Liebi, M., Lennart B.M. and Nygard, K. (2015). Controlling Orientational and Translational Order of Iron Oxide Nanocubes by Assembly in Nanofluidic Containers. *Langmuir*, 31(45): 12537-12543.
<https://doi.org/10.1021/acs.langmuir.5b03678>
- Bandosz, T.J. and Petit, C. (2011). MOF/graphite oxide hybrid materials: exploring the new concept of adsorbents and catalysts. *Adsorption*, 17: 5-16
- Bose, A. and Ma, P. (2019). Mechanochemistry of supramolecules, *Beilstein Journal of Organic Chemistry*, 15: 881-900 DOI: 10.3762/bjoc.15.86
- Chakrabarty, R., Mukherjee P. S. and Stang, P. J. (2011). Supramolecular Coordination: Self-Assembly Finite Two-and ThreeDimensional Ensembles. *Chemical Reviews*, 111: 6810-6918 dx.doi.org/10.1021/cr200077m
- ChandanDey, C., Kundu, T., Biswal, B. P., Mallick, A. and Banerjee, R. (2014). Crystalline metal-organic frameworks (MOFs): synthesis, structure, and function. *Structural Science Crystal Engineering Materials*, 70(1): 3-10. DOI:10.1107/S2052520613029557

- Chih-Chieh, W., Szu-Yu, K., Chia-Wen, C., Yu-Wen, W., Hsiao-Shan, C., Yu-Chien, K., Ning-Kuei, S., Mei-Lin, H., Chung-Kai, C., Yu-Chun, C. and Gene-Hsiang, L. (2017). Four Mixed-Ligand Zn(II) Three-Dimensional Metal-Organic Frameworks: Synthesis, Structural Diversity, and Photoluminescent Property. *Polymers /Basel.*, 9(12): 644-
Doi: [10.3390/polym9120644](https://doi.org/10.3390/polym9120644)
- Christian, B., Cimino, R.T., Gor, G. Y., Neimark, A.V. and Reichenauer, G.(2016). Deformation of microporous carbons during N₂, Ar and CO₂ adsorption: Insight from the density theory. *Langmuir*, 32(32): 8265-8274.
<https://doi.org/10.1021/acs.langmuir.6b02036>.
- Foo, K.Y. and Hameed, B.H. (2010). Insights into the modeling of adsorption isotherm systems. *Chemical Engineering Journal*, 156: 2–10
- Gawas, U. B., Verenkar, V. M. S. and Moju S.C.(2012). Nano-crystalline Mn_{0.3}Ni_{0.3}Zn_{0.4}Fe₂O₄ obtained by novel fumarato-hydrazine precursor method Synthesis, characterization, and studies of magnetic and electrical properties. *Journal of Thermal Analysis and Calorimetry*, 108(3): 865-870
<https://doi.org/10.1007/s10973-012-2387-2>
- Guo, J., Tardy, B. L., Christofferson, A. J., Dai, Y., Richardson, J. J., Zhu, W., Hu, M., Ju, Y., Cui, J., Dagastine, R. R., Yarovsky, I. and Caruso, F. (2016). Modular assembly of superstructures from polyphenol functionalized building blocks. *Nat. Nanotechnol.*, 11: 1105.
- Ion, A.E., Nica, S., Madalan, A.M., Shova, S., Vallejo, J., Julve, M., Lloret, F. and Andrus, M. (2015). Two-Dimensional Coordination Polymers Constructed Using Simultaneously, Linear and Angular Spacers and Cobalt(II) Nodes. New Examples of Networks of Single-Ion Magnets. *Inorganic Chemistry*, 54: 16-18
[dx.doi.org/10.1021/ic5025197](https://doi.org/10.1021/ic5025197)
- Jiang, H.L., Liu, B., Ya-Qian L., Kuratani, K., Akita, T., Shioyama, H., Zong, F. and Xu, Q.(2011). From Metal-Organic Framework to Nanoporous Carbon: Toward a Very High Surface Area and Hydrogen Uptake. *J. Am. Chem. Soc.*, 133: 11854–11857
[dx.doi.org/10.1021/ja203184k](https://doi.org/10.1021/ja203184k)
- Jiang, J. and Yaghi, O.M.(2015). Bronsted Acidity in Metal–Organic Frameworks. *Chemical Reviews*, 115: 6966–6997. DOI: 10.1021/acs.chemrev.5b00221
- Jin, Y., Wang, Q., Taynton, P. and Zhang, W. (2014). Dynamic Covalent Chemistry Approaches toward Macrocycles, Molecular Cages, And Polymers. *Acc. Chem. Res.*, 47: 1575-1586. [dx.doi.org/10.1021/ar500037v](https://doi.org/10.1021/ar500037v)
- [Kumar, P.](#), [Abuhimd, H.](#), [Wahyudi, W.](#), [Li, M.](#), [Ming, J.](#) and [Lain-Jong L.](#)(2016). Review—Two-Dimensional Layered Materials for Energy Storage Applications. *ECS J. Solid State Sci. Technol.*, 5(11) : Q3021-Q3025, Y7; doi:10.1149/2.0181611jss.
- Kupgan, G., Abbott, L.J., Hart, K.E.and Coray, M.C. (2018). Modeling Amorphous Microporous Polymers for CO₂ Capture and Separation. *Chemical Reviews*, 118(11): 5488-5538
- Landers, J., Gor, G.Y. and Neimark, A.V. (2013). Density Functional theory methods for characterization of porous materials. *Colloids and Surfaces A: Physicochemical and Engineering Aspects*, 437: 3-32
<https://doi.org/10.1016/j.colsurfa.2013.01.007>

- Li-Hua W. and Peng-Fei L. (2018). Synthesis, Structure, and Catalytic Activity of A New Mn(II) Complex with 1,4-Phenylenediacetic Acid and 1,10-Phenanthroline. *Bulletin of Chemical Reaction Engineering & Catalysis*, 13(1): 1-6. DOI: <https://doi.org/10.9767/bcrec.13.1.975.1-6>
- Lowell, S., Shields, J. E., Thomas, M.A. and Thommes, M. (2006). Characterization of Porous Solids and Powders: Surface Area, Pore Size and Density. *Springer Science and Business Media LLC*, 1-350
- Lv, Y., Shi P., Shen, W., Chen, X. and Zhao, G. (2015). A series of novel Zn(II) and Mn(II) metal-organic frameworks constructed by 2,4-bis-oxyacetate-benzoic acid: syntheses, structures, and photoluminescence. *Science China Chemistry*, 58: 448-456.
- Mbonu, I. J., Abiola, O. K., Ibe, K. A., Ogeleka, D. F., Elemike, E. E. (2020). Synthesis, crystal structure and photoluminescence properties of diaquabis(1,10 phenanthroline, K, N, N')(benzoate K,O)Manganese(II) dihydrate *Organic & Medicinal Chemistry International Journal*, 9(5): 00129-00145 DOI:10.19080/OMCIJ.2020.09.555773
- Mokhat, S. and Mak, J.Y. (2019). Adsorption capacity. *Handbook of Natural Gas Transmission and Processing* (4 ed). 307-348
- Muhammad A.A.M., Chun-Yang Y. and Robert M.S. (2011). Analysis of the Textural Characteristics and Pore Size Distribution of a Commercial Zeolite using Various Adsorption Models. *Journal of Applied Sciences*, 11(21): 3650-3654. DOI: 10.3923/jas.2011.3650.3654
- Oluwaniyi, M., Seredych, M. and Bandosz, T.J. (2013). Enhanced adsorption of hydrogen sulfide on mixed zinc/cobalt hydroxides: Effect of morphology and an increased number of surface hydroxyl groups. *Journal of Colloids and Interface Science*, 405(2): 18-25. doi: 10.1016/j.jcis.2013.05.006.
- Petit, C., Burrell J. and Bandosz T.J. (2011). The synthesis and characterization of copper-based metal-organic framework/graphite oxide composites. *Carbon*, 49(2): 563-572 <https://doi.org/10.1016/j.carbon.2010.09.059>
- Piota, M., Abecassis, B., Brouid, D., Claire Trouflarada, C., Prousta, A. and Izzeta, G. (2018). Control of the hierarchical self-assembly of polyoxometalate-based metallomacrocycles by redox trigger and solvent composition. *PNAS*, 115(36): 8895-8900
- Ravikovitch, P.I., Vishnyakov, A., Rusco, R. and Neimark A.V. (2000). Unified Approach to pore Size Characterization of Microporous Carbonaceous Materials from N₂, Ar, and CO₂ Adsorption Isotherms. *Langmuir*, 16: 2311-2320
- Sasmal, S. H., Halder, A., Shebeeb, K.H., Dey, K. Nadol, A., Ajithkumar T.G., Bedadur, P.R. and Banerjee, R. (2019). Covalent Self-Assembly in two Dimensions: Connecting Covalent Organic Framework Nanospheres into Crystalline and Porous Thin Films. *Journal of American Chemical Society*, 141(51):20371-20379 <https://doi.org/10.1021/jacs.9b10788>
- Seredych, M. and Bandosz, T.J. (2012). Manganese oxide and graphite oxide/MnO₂ composites as reactive adsorbents of ammonia at ambient conditions. *Microporous and Mesoporous Materials*, 150(1): 55-63.
- Shoji, S., Ogawa, T., Matsubara, S. and Tamiaki, H. (2019). Bioinspired supramolecular nanosheets of zinc chlorophyll assemblies.

Scientific reports, 9: 1-8. 14006
<https://doi.org/10.1038/s41598-019-50026-1>

Springer, M.A., Tsai-Jung L., Kuc, A. and Heine, T. (2020). Topological two-dimensional polymers. *Chem. Soc. Rev.* 1-13. DOI: 10.1039/c9cs00893d

Sun, Y., Zhang, F., Jiang, S., Wang, Z., Ni, R., Wang, H., Zhou, W., Li, X. and Stang, P. J. (2018). Assembly of Metallacages into Soft Suprastructures with Dimensions of up to Micrometers and the Formation of Composite Materials. *Journal of American Chemical Society*, 140: 17297-17307.

Tahier, T. and Oliver, C.L. (2015). In situ Variable-temperature single-crystal X-ray diffraction studies of the single-crystal-to-single-crystal dehydration and rehydration of a mixed-ligand 2D zinc metal-organic framework using trimesate and 4,4'-bipyridine-,'-dioxide as ligands. *CrystEngComm*, 17: 8946-8956
DOI: [10.1039/C5CE01297J](https://doi.org/10.1039/C5CE01297J)

Wu, H. B., Wen, X. and Lou. D. (2017). Metal-organic frameworks and their derived materials for electrochemical energy storage and conversion: Promises and challenges. *Science Advances*, 3: eaap9252, 1-16.

Yu-Ling, L., Zhao, Y., Wang, P., Yan-Shang, K., Liu, Q., Xiu-Du, Z. and Wei-Yin, S. (2016). Multifunctional Metal-Organic Frameworks with Fluorescent Sensing and Selective Adsorption Properties. *Inorganic Chemistry*, 55(22): 11821-11830.
<https://doi.org/10.1021/acs.inorgchem.6b01869>

Zhang, S. (2003). Fabrication of novel biomaterials through molecular self-assembly. *Nature Biotechnology*, 10, pp. 1171-1178 DOI:10.1038/nbt874

Zhao, Y., Song, Z., Li, X., Sun, Q., Cheng, N., Lawes, S. and Sun, X. (2016). Metal-organic frameworks for energy storage and conversion. *Energy Storage Materials*, 2: 35-62. DOI: 10.1016/j.ensm.2015.11.005